IEEE Access
Multidisciplinary | Rapid Review | Open Access Journal

Received 26 April 2024, accepted 24 May 2024, date of publication 3 June 2024, date of current version 14 June 2024.

Digital Object Identifier 10.1109/ACCESS.2024.3408639

RESEARCH ARTICLE

High Voltage-Gain Common-Ground Three-Port DC-DC Converter With Low Current Ripples on the PV Source for Standalone Applications

SIROOS JALILYAN[1], VAHID ABBASI[1], ABBAS RAHIMI VARMENJEH[1], SINA AHMADIAN[1], AND SAMAN A. GORJI[2], (Senior Member, IEEE)

[1]Department of Electrical Engineering, Kermanshah University of Technology, Kermanshah 6715685420, Iran
[2]Faculty of Science Engineering and Built Environment, Deakin University, Burwood, VIC 3125, Australia

Corresponding author: Saman A. Gorji (saman.asgharigorji@deakin.edu.au)

This work was supported by the Commonwealth Scientific and Industrial Research Organisation (CSIRO) International Hydrogen Research Fellowship: Integration of Solar-/Wind-Based Microgrids with Hydrogen Cycle Systems under Grant C041545.

ABSTRACT This paper introduces a three-port DC-DC converter (TPC) designed for enhanced voltage-gain applications. The TPC features two input ports, including a bidirectional port for charging and discharging a battery. It incorporates a switched inductor to achieve higher voltage gains. The converter is capable of operating in four modes, one of which is a battery-alone mode. Compared to existing topologies, the proposed design significantly reduces the ripple of the input current and ensures a common ground connection between the input and output ports. This configuration makes the TPC particularly suitable for renewable energy applications. The functionality and effectiveness of the proposed converter are validated through an experimental prototype with a power of around 400 W. The experiments verified the dynamic performance of the converter during load step changes and mode transitions.

INDEX TERMS Dc-dc converter, nonisolated, standalone, three-port.

I. INTRODUCTION

Alternate energy from renewable sources and their low voltage are their main disadvantages, causing limitations in applications and a reduction of reliability and certainty in supporting power [1], [2], [3]. A high step-up converter and energy storage (ES) should be utilized in conjunction with the sources to improve their performance from the point of view [4], [5].To use renewable energy sources (RES) and ES simultaneously, the system requires two individual converters, which makes the system large and expensive. Integrating RES and ES by multi-port converters (MPC) solves the problems as considered in the recent literature [6]. To present MPCs, it is vital to highlight some of their benefits, like their smaller size, improved dynamic performance, and cost-effective architectures [1], [2], [3], [4], [5], [6], [7]. The presented MPCs are non-isolated, partly isolated, and isolated converters. The non-isolated MPCs have compact configurations compared to the isolated and partly isolated types due to sharing their components in operation modes. The isolated MPCs include single or multi-winding high-frequency transformers that guarantee isolation between the input and the output sides. Although the transformer increases voltage gain related to its turn ratio, these converters contain more semiconductors and components than non-isolated MPCs [6], [7]. In the literature, isolated MPCs are not discussed as often as the non-isolated kind, which is the subject of this work. Even though non-isolated configurations have limitations in some applications, they have been used in stand-alone PV/battery systems. The authors have presented MPCs with three ports (TPC) and four ports converters due to their suitability for renewable applications. Three-port converters have been introduced commonly for use in PV/battery systems to increase the reliability of the load

The associate editor coordinating the review of this manuscript and approving it for publication was Vitor Monteiro.

© 2024 The Authors. This work is licensed under a Creative Commons Attribution-NonCommercial-NoDerivatives 4.0 License.
For more information, see https://creativecommons.org/licenses/by-nc-nd/4.0/

supply in different conditions. A bidirectional port must be prepared in TPC configurations for charging and discharging the energy storage to utilize the full capacity of PVs and the additional power in case of an input power shortage. According to the previous kinds of literature, different quality factors can be defined for MPCs, such as the existence of common ground between the ports and load, the number of operation modes, the level of boosting voltage per the modes, continuity of input current, the low ripple of input current and existence of a bidirectional port to charge/discharge energy storage. For instance, the converters in [8], [9], and [10] do not contain a ground between the input ports and the load due to utilized methods in them, which would be reasons for the limitation. Although preparing a bidirectional port is an important point to supply power with high reliability in renewable energy applications, some of the converters consisting of this feature cannot operate in battery-alone mode as the ones in [10], [11], [12], [13], and [14]. This issue leads to shutting down the converter and cancelling the power transfer when the input power of the main source is zero. Furthermore, some of the presented MPCs [9], [15], [16] do not include a bidirectional port, and they will show more uncertainty in supporting output power that limits their applications. The multi-port converters in [12] and [15] require large inductances for the series inductors with the input source to limit input current ripple, causing higher power loss, lower efficiency, and more effects of parasitic resistance. Adding a port in MPCs and increasing their voltage gain are related to the increase in the number of elements, which leads to caution in designing such converters. Therefore, some of the presented converters have been based on simple converters such as boost, buck-boost, and SEPIC [17], [18], [19], which consist of a limited number of elements but cannot boost voltage appropriately. This challenge can be the focus of further research so that a smaller number of elements can propose a multi-port converter with a suitable voltage gain. Although using a limited number of power switches and diodes is the other point that should be considered when designing MPCs, they must be utilized for performing different operation modes. The point has not been reflected in some converters, such as the ones in [12], [15], [20], and [21], which have many switches and diodes with complex control and high losses. It needs to be mentioned, however, that some of these concerns are interconnected and cannot be considered simultaneously. In this paper, a new circuit has been designed to address most of these concerns. The converter comprises three ports, one of which is a bidirectional port to charge and discharge a battery. Its performance has been performed for four operation modes, including battery-alone mode, and the converter can supply the load by unbalanced powers of the input ports. In addition, the TPC boosts voltage with high gains in the main operating modes, and it continuously transfers current from the input source. The configuration includes a common ground between the ports and the load that increases its applications. An effective switching strategy is defined as one that needs a simple system for shifting between the operations modes. The switching strategy makes the possibility of controlling the input power of the source and output voltage. According to the mentioned quality factors of the converter and its superiorities compared to the references, the components have been used suitably in the configuration, respecting the number of them. The proposed converter offers several advantages:

- Continuous current of primary input(PV)
- Low input current ripple
- High voltage gain
- Bidirectional port for battery charging and discharging
- Common ground between ports

The properties and performance of the proposed converter are studied in different sections of the paper. The converter configuration converter and its operation modes are described in Sections II and III. The converter properties are compared with the other converters in Section IV. Sections V and VI include a description of the control system and experimental verifications, respectively. In addition, Section VII concludes the proposed TPC.

II. THE PROPOSED CONVERTER AND ITS ANALYSIS

In general, three methods have been used to transfer power from the input ports to the loads in multiport converters. In summary, the currents of the input ports at a connection point are used in the first method, where series diodes with the sources should be utilized, such as the converters presented in [19], [21], and [22]. Fig. (1)(a) illustrates the introduced method and location of the diodes. In this method, if required, both sources flow current through the (a) point simultaneously, it is obligatory to regulate the (a) point's voltage in the way that two diodes will be on. On the other hand, two sources must set the (a) point's voltage at the same value. Otherwise, during a part of the switching cycle, the diode of the first source will be on, and in other switching parts, the diode of the second source will be on and the power control will be complicated. The second method is based on power transferring from the input sources by the sum of their voltages in common loops like the proposed converters in [9], [10], [12], and [23]. This method increases the voltage gain, in addition to the introduced power transfer. In some operation modes, the mentioned structure increases the input current ripple, and an increase in current passes through the components occurs. Therefore, converters need larger inductors to limit the high current ripple and used components with higher nominal currents to avoid damage by high current stress. Summing up the powers of the input sources with their independent performance is another method used in some converters, such as [24], [25], and [26]. These converters require power to transfer simultaneously from both input sources Fig. (1)(c). If the performance consists of boosting input voltage, two independent step-up units must be used for both parts of the converter, meaning an increase in the number of used components. This article utilizes a new method to combine the input powers of the sources and does not follow

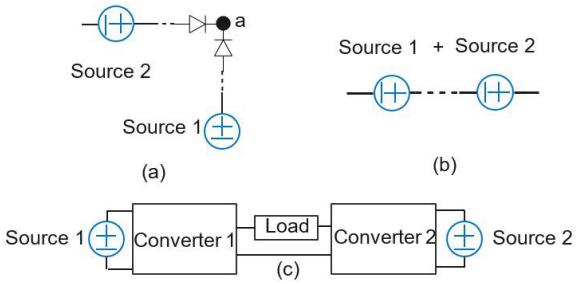

FIGURE 1. Methods of power-sharing between the input sources in MPCs (a) the first method (b) the second method (c) the third method.

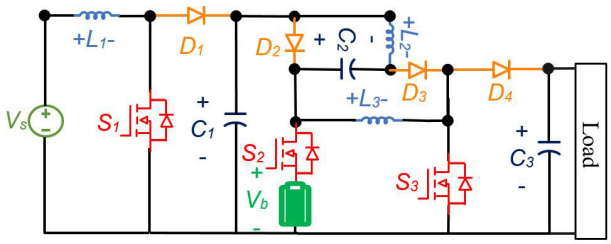

FIGURE 2. Structure of the proposed converter.

the previous solutions. The output voltage will result from the voltages of capacitors and inductors in the circuit loops, causing the independent performance of the sources. The method does not transfer power by summing up the sources' voltages or currents. This feature can be explained while investigating the converter's operation modes.

A. CONFIGURATION OF THE PROPOSED CONVERTER

The proposed converter includes two input ports and an output port for connecting to the load. One of the ports has been developed to be a bidirectional port to charge and discharge the battery and the other port is unidirectional to transfer the power of the renewable energy source. The ports are unified with a switched inductor (SI) to boost voltage gain, giving the possibility of high gain operation in its operating modes. The presented configuration contains three switches that are used to switch between the modes and control the primary source's output voltage and input power. Notably, an auxiliary inductor can be incorporated into the circuit with C2 for sensitive applications to prevent impulsive charging and discharging of C2 if it risks existing. Fig. (2) illustrates the converter with details of the used components in its structure. A simple control system is needed to regulate the desirable variables due to the use of a small number of switches and the low number of switching states in each operation mode. The converter can operate in four modes related to the power balance between the input source, the battery, and the load. In addition, battery status and voltage have to be considered for the possibility of operation in each mode. The first operation or charging mode occurs when the input power is higher than the output power, and the source can charge the battery with its extra power. The output power is supplied by discharging the battery and power of the input source in the second operation mode, which can be defined as the discharging mode. The discharging performance of the battery depends on its stored energy and voltage, which has to be higher than its minimum value (V_b>V_{bmin}). In the third mode, there is no need to use the battery's stored energy and no additional power to charge it, meaning the battery does not contribute to the performance. The battery can support the load on its own when the input power of the source is equal to zero, which is defined as the battery to determine the mode or the fourth mode. The following section includes a description of the modes' states and an analysis of the modes while the converter's performance occurs in continuous conduction mode (CCM).

III. THE OPERATION MODES AND THEIR ANALYSIS

The modes are studied by the drawn fundamental waveforms in Fig. (4), which shows the modes include a maximum of four switching states.

A. THE FIRST OPERATION MODE (CHARGING MODE)

This mode has three states with equivalent circuits as shown in the (3) and its time intervals change from t_0 to t_4. In the first state (t_1< t < t_2), the only conducting switch is S1 such as shown in the Fig.3. The input source energizes L_1, and its current increase linearly Fig. 4 while the diode D_1 is blocked. Using Fig. 3(a), the following equation can be written.

$$V_s = V_{L_1}. \tag{1}$$

The capacitor C_3 is charged by L_2, C_3, C_1, and C_2 through D_4, and the other diodes D_2 and D_3 are blocked. The introduced components form a loop, which is the base of (2).

$$V_{C_1} + V_{C_2} - V_{L_2} - V_{L_3} = V_O. \tag{2}$$

By equating $V_{L_2} = V_{L_3}$ (this can be proven based on analysis of SI's circuit), the equation (2) is rewritten as:

$$2V_{C_1} - 2V_{L_2} = V_O. \tag{3}$$

$$V_{L_2} = \frac{2V_{C_1} - V_O}{2}. \tag{4}$$

The equivalent circuits of the converter per two of the other states ($t_2 < t < t_3$) and ($t_4 < t < t_0$) are similar as depicted in the Fig. 3(b). There is no need to turn on the switches and L_1 charges C_1 through D_1. Referring to the Fig.3(b), the equation (5) can be extracted.

$$V_s - V_{L_1} = V_{C_1} \tag{5}$$

According to the key waveforms of the Fig. 4(a),(1) and (5), voltage-second balance theory for L_1 can be extracted as (6).

$$D_1 V_s + (1 - D_1)(V_s - V_{C_1}) = 0 \tag{6}$$

Thus, voltage of C_1 is obtained from (6).

$$V_{C_1} = \frac{V_s}{(1 - D_1)} \tag{7}$$

The remaining state occurs in a time interval as t_3< t <t_4 when S_2 and S_3 are turned on, unlike S_1 which is off. The battery is charging by the powers of the input source and C_1 due

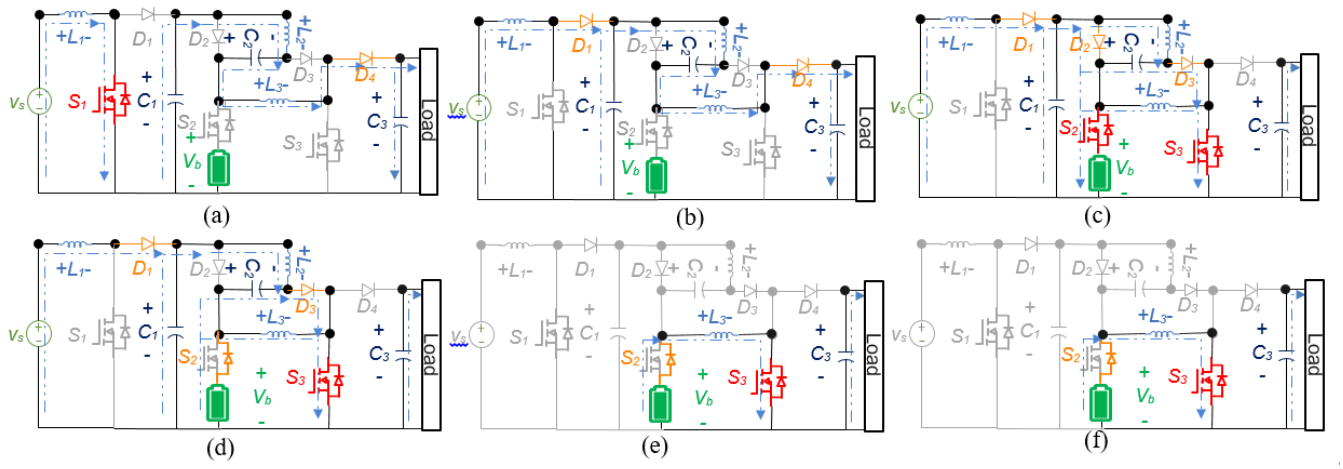

FIGURE 3. Switching states of the first and second operation modes (charging and discharging modes) (a) $t_1 < t < t_2$, (b) $t_4 < t < t_0$ and $t_2 < t < t_3$, (c) $t_3 < t < t_4$ in the first operation modes(charging mode) (d) $t_3 < t < t_4$ in the second operation modes (discharging modes) Switching states of the fourth operation modes (battery alone modes) (e) $t_0 < t < t_1$, (f) $t_1 < t < t_2$.

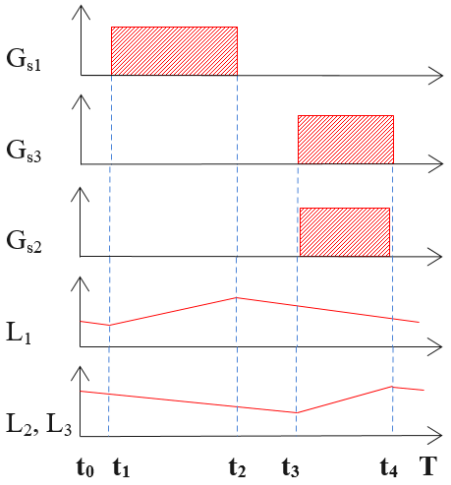

FIGURE 4. Key waveforms of the proposed converter the first, the second and the third modes.

to formation of a power-transferring path through D_2 and S_2 such as shown in Fig. 4(c). In charging mode, there is a basic condition between the voltage of the battery and the voltage of C_1 which is definable by $V_{C_1} > V_b$. This inequality equation implies the dependence between this mode and the battery status. The inductors of SI (L_2 and L_3) and C_2 are charging by the input source and L_1 in the loops consisting of D_2, D_3 and S_3. Using analysis of this state, the relations between the voltage of L_1, L_2, C_1 and C_2 are as

$$V_{C_1} = V_{L_2} = V_{L_3} \tag{8}$$

$$V_{C_1} = V_{C_2} \tag{9}$$

Similarly, voltage-second balance theory for L_2 is obtained as shown in (2) and (2) which indicates the relation between output voltage and V_{C_1}.

$$D_3 V_{C_1} + (1 - D_3)\left(\frac{2V_{C_1} - V_O}{2}\right) = 0 \tag{10}$$

$$V_O = 2\frac{V_{C_1}}{(1 - D_3)} \tag{11}$$

Substituting (7).into (11). gives voltage gain of the converter in charging mode.

$$V_O = \frac{2}{(1 - D_1)}\frac{V_S}{(1 - D_3)} \tag{12}$$

B. THE SECOND OPERATION MODE (DISCHARGING MODE)

The key waveforms of this mode would be like Fig. 4(a) with the difference that S_2 does not receive PWM pulse, and it is turned off. As it can be understood from the converter's configuration, the voltage of the battery must be higher than V_{C_1} for the discharge the battery is possible. Some of the states in this mode are as same as the ones in the charging mode such as the states in time intervals including $t_0 < t < t_3$ and $t_4 < t < t_0$. Therefore, the equations (1), (2), (5), (6) and (7) are also valid for this mode. As shown in Fig. 3(d), the different state occurs during $t_3 < t < t_4$ when the battery discharges through the body diode of S_2. In this state, battery is used to energize L_3 and C_2 in the loops consisting of S_2's diode (D_{S_2}), S_3 (first loop) and D_{S_2}, D_3 and S_3 (second loop) respectively. Furthermore, L_2 is charged by the input source, L_1 and C_1 through the formed current paths by D_1, D_3 and S_3. According to Fig. 3(d), voltage of C_2 and L_3 are equal to V_b ($V_b = V_{C_2} = V_{L_3}$) and $V_{C_1} = V_{L_2}$. By using volt-balance theory, a relation such as (10) can be written which is summarized to obtain output voltage (V_O).

$$D_3(V_{C_1} + V_b) + (1 - D_3)(V_{C_1} + V_b - V_O) = 0 \tag{13}$$

$$V_O = \frac{V_{C_1} + V_b}{(1 - D_3)} \tag{14}$$

Substituting (7) into (42), shown at the bottom of page 12, gives V_O related to V_B and V_S.

$$V_O = \frac{V_S + V_b(1 - D_1)}{(1 - D_1)(1 - D_3)} \tag{15}$$

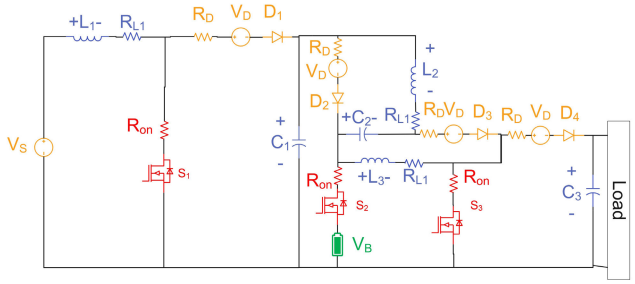

FIGURE 5. Non-ideal structure of the proposed converter.

C. THE THIRD OPERATION MODE (NO BATTERY CONTRIBUTION)

This mode includes the states similar to the charging mode and the only difference is in operation of S_2. Due to no contribution of the battery in the third mode, the switch (S_2) should be turned off during this mode, and (V_{C_1}) > (V_b). Analysis of the converter would be the same as a simple circuit, and its voltage gain can be obtained as written in (14).

$$V_O = \frac{2V_S}{(1-D_1)(1-D_3)} \tag{16}$$

D. THE FOURTH OPERATION MODE (BATTERY ALONE MODE)

The performance of the converter has two states in this mode, as shown in 3 Because of no power transferring from the input source, there is no need to use S_1, and S_3 is the only active power switch, as shown in 4(b). According to3(e), all the semiconductors except D_4 are blocked during t_0< t <t_1 and the battery transfers its power to the load through the body diode of $S_2(D_{S_2})$ and D_4. In addition, L_3 assists the battery by its discharging and supporting the load and energizing the output capacitor (C_3). As shown in Fig. 3(f), an equation such as (17) can be derived.

$$V_b - V_{L_3} = V_O \tag{17}$$

In the $t_1 < t < t_2$, the switch S_3 is the only conducting one that prepares a current path for charging L_3. Thus, in this state, the inductor's voltage is equal to V_b ($V_b = V_{L_3}$). Using the voltage of L_3 per the states, the volt-balance equation of the inductor can be written as follows.

$$d_3(V_b) + (1-D_3)(V_b - V_O) = 0 \tag{18}$$

Output voltage of the converter is extracted from ((18)) as:

$$V_O = \frac{V_b}{(1-D_3)} \tag{19}$$

E. NON-IDEAL VOLTAGE GAIN FOR PV ALONE MODE

Fig. 5 is considered a non-ideal circuit for the proposed converter. The same analysis in the previous section was performed in PV alone mode to obtain the proposed converter's non-ideal voltage gain. To simplify the equation, all inductor resistance (r_L), switch-on resistance ($r_o n$), diode resistance (r_d), and diode voltage forward (v_D) are equal.

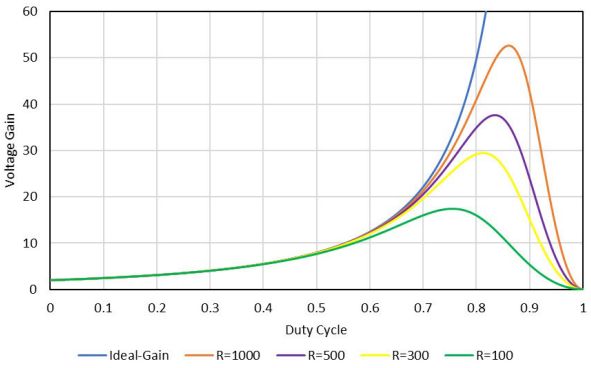

FIGURE 6. Non-ideal voltage gain and real voltage gain (the values of r_L=.02, rd=0.007, R_{on}=.08, v_d=0.6).

Additionally, analogous analyses can be conducted for the non-ideal voltage gain of the other operational modes. non-ideal voltage gain is shown in eq (20), as shown at the bottom of the next page, and the ideal and the non-ideal voltage gain are plotted in Fig. 6 for different output loads It should be noted that the parasitic values are considered as r_L=.02, rd=0.007, R_{on}=.08, v_d=0.6.

Semiconductor stresses, including voltage and current stress of switches and diodes, are shown in Table 1.

TABLE 1. Semiconductores Stresses in PV alone mode.

Component	Voltage stress	Current stress
S_1	$\frac{(1-D_3)v_O}{2}$	$\frac{2v_O}{(1-D_1)(1-D_3)R}$
S_2	$\frac{(1+D_1)(1-D_3)v_O}{2} - V_b$	$\frac{v_O}{(1-D_3)R}$
S_3	v_O	$\frac{2v_O}{(1-D_3)R}$
D_1	$\frac{(1-D_3)v_O}{2}$	$\frac{2v_O}{(1-D_1)(1-D_3)R}$
D_2	$\frac{1-D_3{}^2 v_O}{2}$	$\frac{v_O}{(1-D_3)R}$
D_3	$\frac{1-D_3{}^2 v_O}{2}$	$\frac{v_O}{(1-D_3)R}$
D_O	v_O	$\frac{v_O}{(1-D_3)R}$

IV. COMPARISON WITH THE OTHER CONVERTERS

Based on the paper title, three-port converters are utilized as the primary references for comparisons. Most of the converters in Table 2 contain three ports and two of them have four ports. Table 2covers the quantitative and qualitative properties of the converters, which can help to introduce the proposed converter's advantages and disadvantages. According to the details, the converters in [10], [11], [12], and [27] have at least one not common grounded input port, meaning limitation in their applications. Most of the converters include main input ports with continuous input current except the one in [10]. The other quality factor related to renewable sources (RS) is input current ripple which must be considered during the design of the converters. According to the current ripple equations in Table 2, the proposed converter, and the converters in [13] and [15] transfer power from RS with the lowest ripples (Fig. 7). The current ripple in [11], [12], and [27] is high due to the use of unsuitable methods in power sharing, as discussed

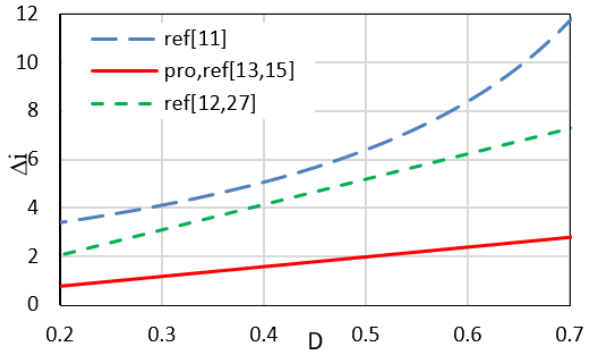

FIGURE 7. δi of the converters versus duty cycle (ref [10] is discontinues).

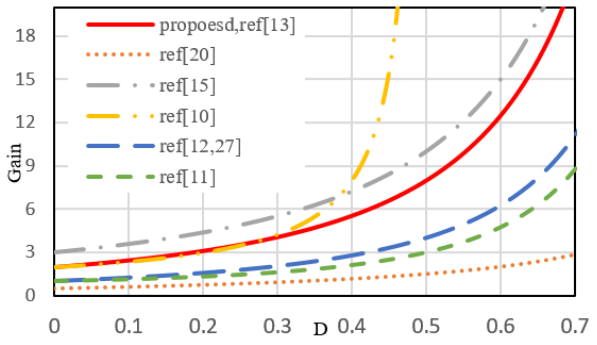

FIGURE 8. Voltage gains of the converters versus duty cycles (different duty cycles of the converters are assumed similar $d_1 = d_2$).

in section II. Referring to the curves in Fig. 7, the current ripple in the proposed converter is lower than 20% until D= 0.5. In addition, the maximum of the current ripple in the proposed converter is lower than 30% for similar conditions (the input voltage, size of the series inductor with the input source, and frequency are assumed 20V, 100 μH, and 50 kHz, respectively). It must be noticed, that the converter in [10] transfers power with discontinues input current.

Various points have been considered in the presentation of the proposed converter to cover the limitations of the previous cases and introduce a converter with more advantages. The proposed converter is designed to have a low number of semiconductors which causes higher efficiency. To verify the issue, the maximum efficiency and efficiency of the converters in their nominal power are listed in the last column of Table 1. The proposed converter operates with the highest efficiency (94%) per its nominal power (420W) in comparison to the references. In addition, its maximum efficiency has a high value similar to [10], [12], [13], and [15]. Thus, the results demonstrate the high-efficiency performance of the converter in both points of the comparison. The number of operation modes in MPCs can be considered as a factor to investigate the flexibility and reliability of their performance, especially when the input sources do not have enough certainty in supplying the load. The problem can be resolved by setting up a bidirectional port for charging and discharging the battery storage. In addition, the converters can handle the situation better when there is a possibility of operation in the battery-alone mode with the bidirectional port. Although all the converters except the converter in [15] have a bidirectional port, none of them can support the load in battery-alone mode except the proposed one. This advantage (operation in stand-alone mode) results from well designing and localization of the bidirectional ports for the proposed converter. In addition, the converter presents this property with an acceptable number of used components (the total number of components (T) in the proposed converter is 13). Furthermore, the converter boosts voltage by high gain during the operation modes. Using the voltage gain equations in Table 2, the converters have been compared from this point of view in Fig. 8. Besides the other positive points of the proposed converter, its voltage gain is higher than the converters in [11], [12], [20], and [27]. Although the converter in [15] operates with a higher voltage gain, it does not include a bidirectional port despite using three extra components consisting of six power switches. The cost comparison is shown in Table 4, demonstrating that the proposed converter has a lower price point than most other converters, except [12]. Notably, [12] boasts an output power of approximately 100 watts, and its switches and diodes are equipped with lower nominal power ratings, thus contributing to their lower prices. Importantly, it should be emphasized that the output power of the proposed converter stands at around 400 watts, surpassing that of the other compared converters. However, despite these factors, the lower pricing of the proposed converter's other components, such as the Inductor, enables its final price to remain competitive with [12] and even lower than the prices of the other compared converters. When comparing the efficiency of the proposed converter, it is important to note that the output power range of the proposed converter is greater than that of the compared converters. Like converters [10], [12], and [15], the proposed converter achieves high maximum efficiency, which is nearly equal to those converters and higher than converters [11], [13], and [27]. Additionally, the proposed converter has a narrower efficiency range within the tested output power range compared to converters [11], [15], and [27], and it maintains a higher minimum efficiency than converters [11], [15], and [27].

V. CONTROL ALGORITHM

The proposed TPC is controlled based on a designed control algorithm, as illustrated in Fig.9. The first step of the

$$\frac{v_O}{v_g} = \frac{1-(1-D_1)^2\frac{v_D}{2v_g}}{(r_L + r_{ON}D_1 + r_D(1-D_1))\left(\frac{(2)}{R(1-D_3)(1-D_1)}\right) + \frac{1}{2}\left(\left(1-D_3+(1-D_3)\frac{r_d}{R} + 2R_{ON}\frac{D_3}{R} + \frac{2r_L}{R}\right)\right)(1-D_1)} \quad (20)$$

TABLE 2. Comparison of the proposed converter with other multiport DC-DC converters (P: ports, S: switch, D: diode, L: inductor, C: capacitor, T: total number of components, PRO*: proposed converter).

REF		[10]	[11]	[12]	[13]	[15]	[27]	Proposed
Voltage gain		$\frac{2-D}{1-2D}$	$\frac{1-D+D^2}{(1-D)^2}$	$\frac{1}{(1-D)^2}$	$\frac{2}{(1-D)^2}$	$\frac{(2-D_1)V_{in_1}}{(1-D_1)^2}+\frac{V_{in_2}}{(1-D_2)^2}$	$\frac{V_{in_1}}{(1-D_1)}+\frac{V_{in_1}+V_{in_2}}{(1-D_2)}$	$\frac{V_{in_1}+(V_{in_2})(1-D_1)}{(1-D_1)(1-D_2)}$
Battery Alone Mode		NO	NO	NO	NO	NO	NO	YES
Common ground		NO	NO	NO	YES	YES	NO	YES
Continuous input current		NO	YES	YES	YES	YES	YES	YES
Bi-dirctionall port		YES	YES	YES	YES	NO	YES	YES
Input Current Ripple Scale		-	$\frac{((V_{in_1}D_1}{1-D_2}+\frac{V_{in_2})D_2)}{Lf}$	$\frac{(V_{in_1}D_2}{+(V_{in_1}+V_{in_2})D_2)}{Lf}$	$\frac{V_{in_1}D_1}{Lf}$	$\frac{V_{in_1}D_1}{Lf}$	$\frac{(V_{in_1}D_1+}{(V_{in_1}+V_{in_2})D_2)}{Lf}$	$\frac{V_{in_1}D_1}{Lf}$
Number of Operation Modes		3	3	3	3	2	3	4
Output power(W)		180	152	100	250	350	80	600
Efficiency		93%-96.5%	<92%	91%-96%	90%-94.2%	85%-96%	90%-92%	91%-96%
Number of Elements	L	2	2	2	4	4	2	3
	C	4	2	2	4	4	2	3
	D	6	4	5	5	2	5	4
	S	4	4	3	4	6	4	3
	T	16	12	12	17	16	13	13

TABLE 3. Cost comparison (S, D, C, L, TC Represent the Switches/Diodes/Capacitors/Inductor/Total Component).

REF		[10]	[11]	[12]	[13]	[15]	Proposed
$P_O(W)$		120(W)	152(W)	100(W)	250(W)	180(W)	400(W)
Cost of Components	L($)	23 $	18 $	18 $	35 $	25 $	13.2$
	C($)	5.8 $	5.8 $	6.6 $	9.1 $	8.32 $	4.27 $
	D($)	7 $	19 $	6.1 $	32.25 $	9.95 $	15.56 $
	S($)	12.28 $	13.68 $	12.28 $	8.2 $	3.28 $	13.37 $
	T($)	48.08 $	56.48 $	42.98 $	84.8 $	46.55 $	46.4$

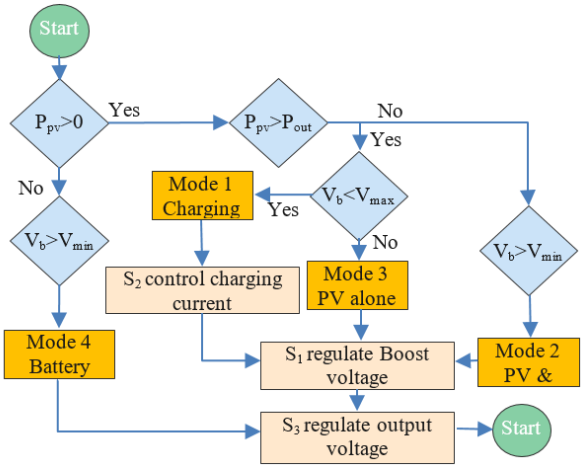

FIGURE 9. Control diagram for the operation modes of the proposed converter.

algorithm includes collecting real-time data by voltage feedback and current sensors. Utilizing the data and comparing output and input power is possible and essential to diagnosing the operation mode. The next unit contains a mode diagnosis for defining operation modes in different conditions. The modes are related to battery voltage status. As an example, when P_{out}<P_{pv} and V_b<V_{bmax}, the input source supplies the load and charges the battery, which is defined with charging mode. In this condition, if the battery voltage status shows that it is higher than its maximum (V_b>V_{bmax}), the input

TABLE 4. Utilized Components in Proposed Converter.

PARAMETERS	Value	PARAMETERS	Value
V_{in}	20V	V_b	48V
Output Voltage	255V	Switching Frequency	50 kHz
L_1	100µH	L_2, L_3	340µH
C_1, C_2,C_3	68µF	S_1	IRF1407
S_2	IRF260N	S_3	2SK3131
D_1, D_2, D_3	SP3004	D_4	DSEC30
R_{out}	80 - 220 ohm		

source (PV) transfers its power to the load as the PV alone mode or the third mode. Performance conditions of the converter for the other modes can be followed using the algorithm in Fig. 9. The last part of the diagram allocates the number of active switches to the distinguished mode. In the end, the controllers regulate PWM signals with suitable duty cycles.

The microcontrollers assign appropriate compensators for various operating modes to control the PWM pulses effectively. Designing a suitable controller maintains stable output voltage load fluctuations and input voltage variations. The state-space average model and small-signal model converter's open-loop transfer function are derived for the discharging mode to facilitate this. Considering the equality of the voltages of capacitors C1 and C2 and the currents of inductors L2 and L3, the number of state variables can be reduced. This simplification can reduce the order of the

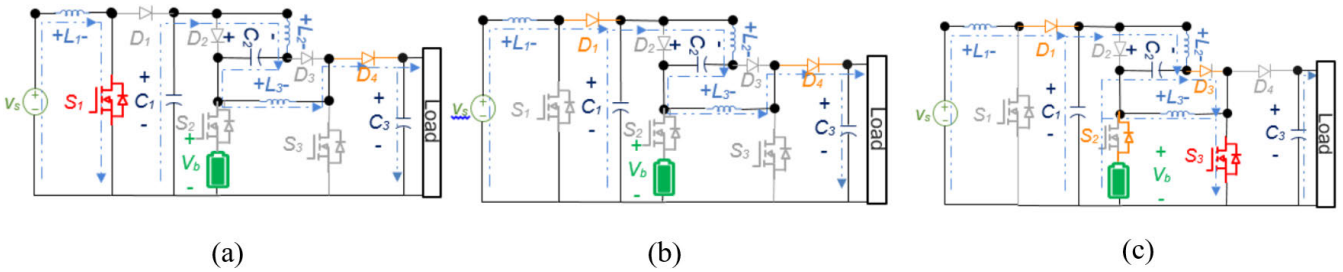

FIGURE 10. Equivalent circuit of the proposed converter for state space analysis in each switching state (a) state 1,(b) state 2, (c) stare 3.

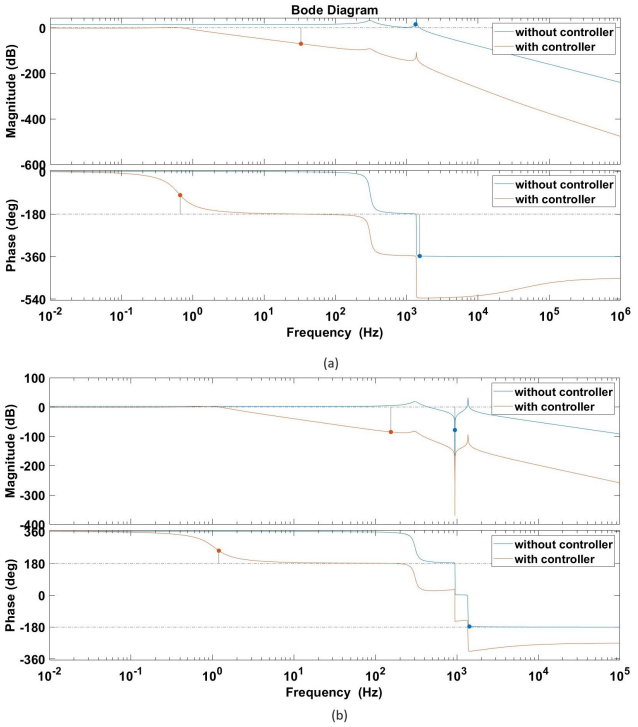

FIGURE 11. Bode diagram of the proposed converter without controller and with controller for a) G_{in1} and b)G_{in2}.

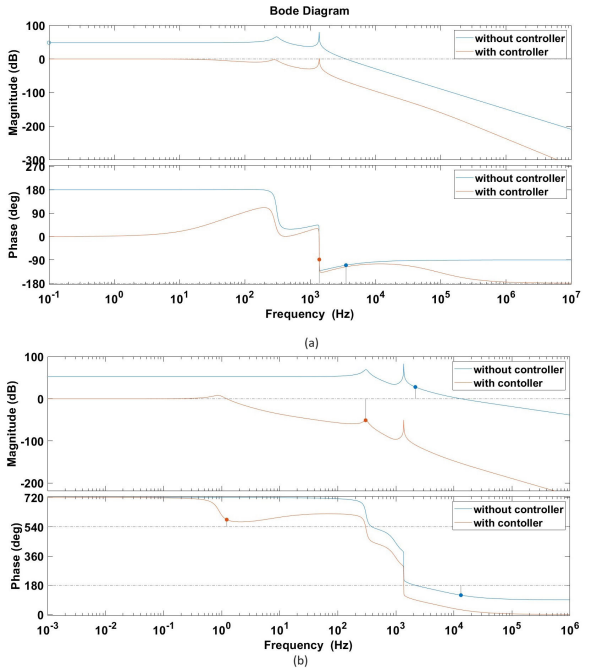

FIGURE 12. Bode diagram of the proposed converter without controller and with controller for a) G_{vd1} and b)G_{vd3}.

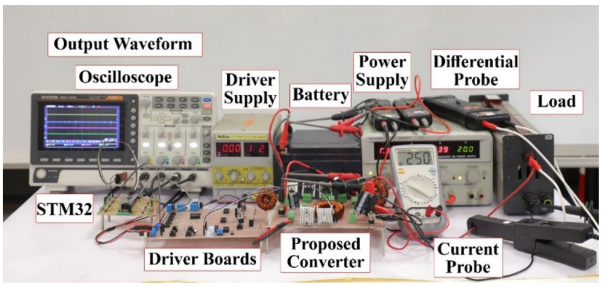

FIGURE 13. Experimental setup.

proposed converter's matrix and create a simpler model. In this analysis, the following parameters are selected as state-space variables.

$$x = [I_{L_1}, I_{L_2}, V_{C_1}, V_{C_O}]' \tag{21}$$

$$\frac{d}{dt}\hat{X} = A\hat{X} + B\hat{U} \tag{22}$$

$$Y = C\hat{X} + D\hat{U} \tag{23}$$

where U is the input matrix. The following section will explain the matrices A, B, C, and D and how to obtain them. Matrices A, B, C, and D have been obtained based on the switching pattern shown in Fig. 4. It should be noted that since the averaging method has been used for the proposed converter's small signal, it is calculated in three intervals. To derive the average and small-signal models, equations for the states need to be derived from the equivalent circuit of the converter, which, shown in Fig. 10., depicts the first, second, and third states of the discharging mode. To obtain the state-space equations, it is necessary to derive the A, B, C, and D matrices, where the matrices resulting from KVL and KCL are in Fig. 10 for state variables such as inductors and capacitors. For every equivalent circuit depicted in Fig. 10., it is essential to derive matrices A, B, C, and D. Subsequently, the average of these three resulting matrices is selected as the

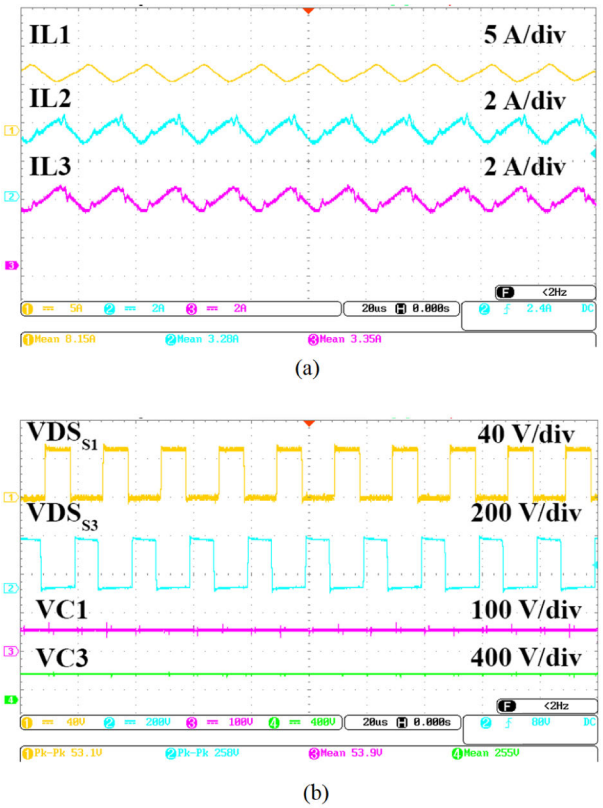

FIGURE 14. Experimental results of the second mode for $P_O = 295$W, $P_PV = 165$W, $P_b = 130$W, $d_1 = 0.59$ and $d_2 = 0.61$ (a) current of L_1, L_2 and L_3 (b) voltage of S_1, S_3, C_1 and C_3.

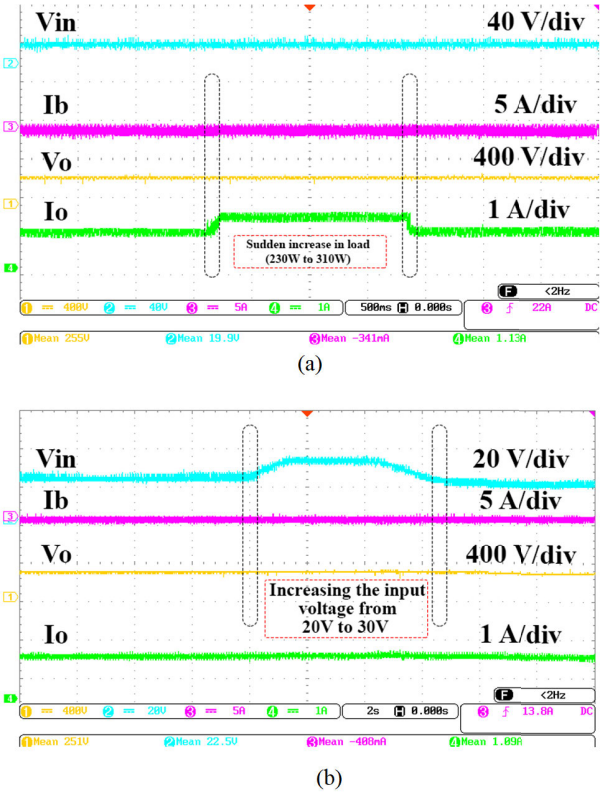

FIGURE 15. Dynamic response of the converter per the first operation mode where the output voltage and current of the battery are controlled (a) variation of output power from 230W to 310W (b) variations of the input voltage from 20V to 30V.

state-space matrix. A, B,C,and D can be written as (24) to (28)

$$A = \begin{bmatrix} 0 & 0 & -\frac{(1-D_1)}{L_1} & 0 \\ 0 & 0 & \frac{1}{L_2} & -\frac{(1-D_3)}{2L_2} \\ \frac{(1-2D_1-2D_3)}{C_1} & -\frac{2-D_3}{2C_1} & 0 & 0 \\ 0 & \frac{(1-D_3)}{C_3} & 0 & -\frac{1}{RC_3} \end{bmatrix} \tag{24}$$

$$B = \begin{bmatrix} \frac{1}{L_1} & 0 \\ 0 & \frac{d_3}{L_2} \\ 0 & 0 \\ 0 & 0 \end{bmatrix} \tag{25}$$

$$C = \begin{bmatrix} 0 \\ 0 \\ 0 \\ 1 \end{bmatrix} \tag{26}$$

$$D = [0\ 0] \tag{27}$$

To obtain a system's transfer function, matrices A, B, C, and D should be into (28). The transfer function representation for a system given matrices A, B, C, and D is given by (28), whereas I in (28) is the identity matrix.

$$G(s) = C(SI - A)^{-1}B + D \tag{28}$$

Based on (24) to (28), the analysis identifies two inputs, denoted as V_{in} and V_b, and one output V_O. The small-signal functions $G_{vg1} = (\frac{V_o}{V_1})$ and $G_{vg2} = (\frac{V_o}{V_b})$ can be written as (29) and (30) respectively.

$$G_{in1} = \frac{1.527e15}{s^4 + 294.1s^3 + 7.768e07s^2 + 2.056e10s + 2.748e14} \tag{29}$$

$$G_{in2} = \frac{1.038e07s^2 - 1.029e - 06s + 3.664e14}{s^4 + 294.1s^3 + 7.768e07s^2 + 2.056e10s + 2.748e14} \tag{30}$$

Like the previous analysis, the input matrix will be changed to obtain a small signal model of the proposed converter.

$$u = \begin{bmatrix} D_1 \\ D_3 \end{bmatrix} \tag{31}$$

By utilizing (24) and substituting D(Duty cycle) to (D+$\hat{d}$),the matrix B for G_{vd} can be derived. This modification affects only matrix B, while matrices A, C, and D remain unchanged.

$$B_{G_{vd}} = \begin{bmatrix} \frac{V_{C_1}}{L_1} & 0 \\ 0 & \frac{V_O}{2L_2} \\ -2\frac{i_{L_1}}{C_1} + \frac{i_{L_2}}{C_1} & -2\frac{i_{L_1}}{C_1} \\ 0 & -\frac{i_{L_2}}{C_3} \end{bmatrix} \tag{32}$$

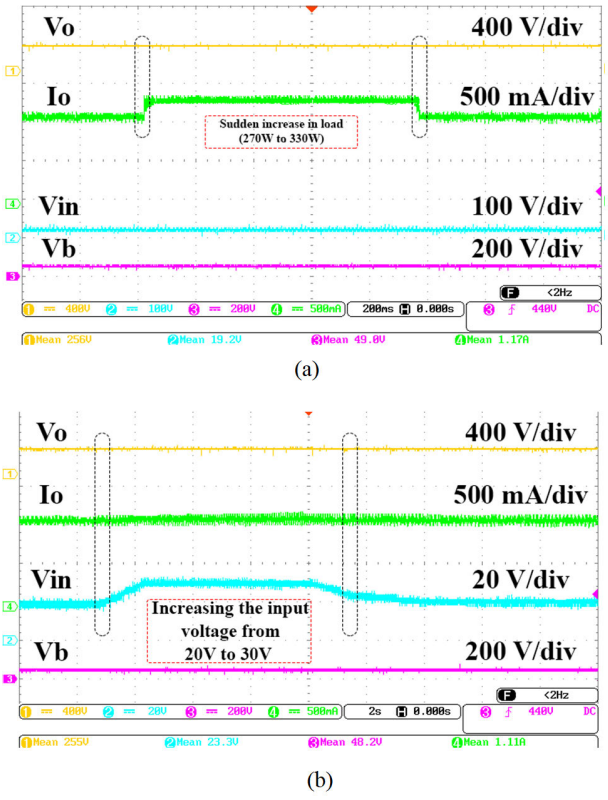

FIGURE 16. Dynamic response of the converter per the second operation mode where the output voltage and current of the battery are controlled (a) variation of output power from 270W to 330W (b) variations of the input voltage from 20V to 30V.

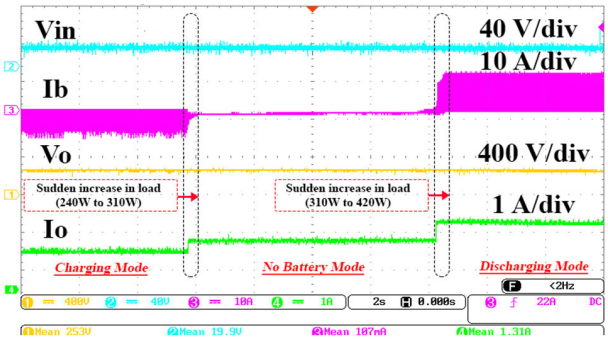

FIGURE 17. Control of the proposed converter during the operation mode variations.

Based on eq(24), (26) to (27) and (32) the small-signal functions $G_{vd1} = (\frac{V_{C1}}{D_1})$ and $G_{vd3} = (\frac{V_o}{D_3})$ can be written as eq(34) and eq(35)

$$G_{vd1} = \frac{-8.587e12s - 7.327e16}{s^4 + 294.1s^3 + 7.768e07s^2 + 2.056e10s + 2.748e14} \tag{33}$$

$$G_{vd3} = \frac{-7.353e04s^3 + 3.309e09s^2 - 1.277e13s + 1.168e17}{s^4 + 294.1s^3 + 7.768e07s^2 + 2.056e10s + 2.748e14} \tag{34}$$

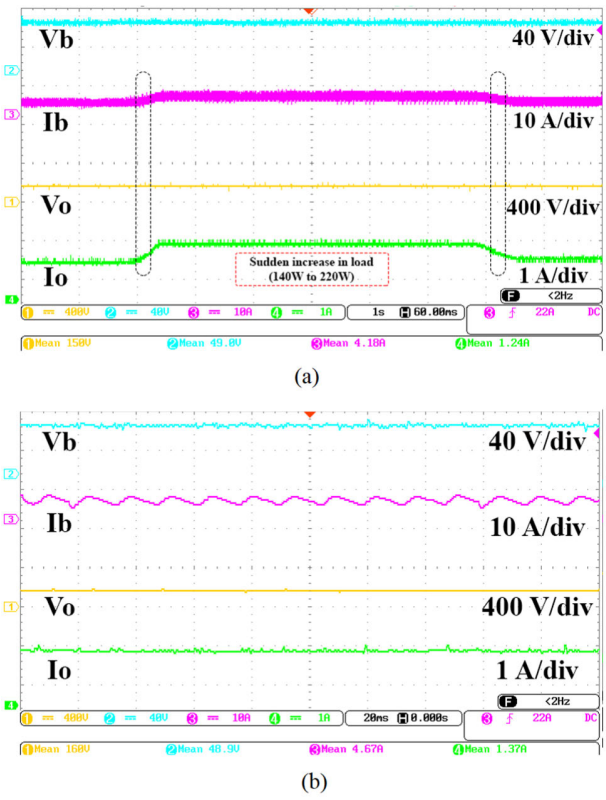

FIGURE 18. Performance of the converter in the fourth mode (battery alone mode) (a) dynamic response of the converter when the output power is varied from 140W to 220W and then from 220W to 140W- V_O = 150V (b) performance of the converter for P_O = 230W.

By utilizing G_{CV1} and G_{CV2} as a controller for G_{in1} and Gin2 respectively, as shown in eq (35) and (36), the closed-loop transfer function of G_{in1} (G_{Clin1}), as shown at the bottom of page 12, and G_{in2} (G_{Clin2}), as shown at the bottom of page 12, for the proposed converter can be derived.

$$G_{CV1} = \frac{4e-06s+1}{0.4278s^2 + 1.31s + 1} \tag{35}$$

$$G_{CV2} = \frac{0.00076s + 8}{0.264s^2 + 1.34s + 1} \tag{36}$$

By utilizing G_{CD1} and G_{CD2} as a controller for G_{vd1} G_{vd2}, as shown in eq(39) and eq(40), the closed-loop transfer function of G_{vd} and (G_{CLvd1}), as shown at the bottom of page 12, and G_{vd1} and (G_{CLvd3}), as shown at the bottom of page 12, for the proposed converter can be derived.

$$G_{CD1} = \frac{0.025s + 1}{13.4s^2 + 20.67s + 1} \tag{39}$$

$$G_{CD2} = \frac{0.00068s + 1}{2.7e-6s^2 + 1.5s + 1} \tag{40}$$

Fig. 11 illustrates bode diagrams of G_{in1} and G_{in2} with and without controller. The results show that for Fig. 11 (a) phase margin (PM) is changed from $-180°$ to $80°$. In addition, the controller improves the gain margin (GM) by changing it from -15 dB to 70 dB. Furthermore Fig. 11 (b) show that for G_{vg2} phase margin (PM) is changed from $3.29°$ to $71.5°$. In addition, the controller improves the gain margin (GM) by

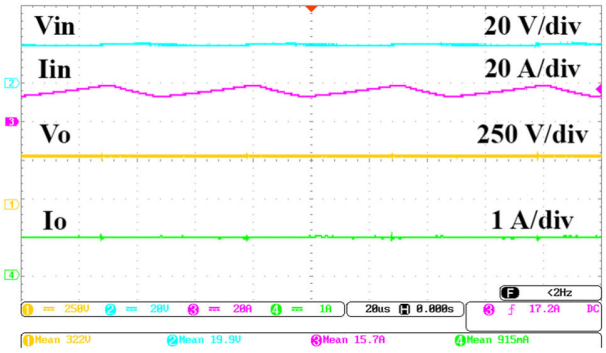

(a)

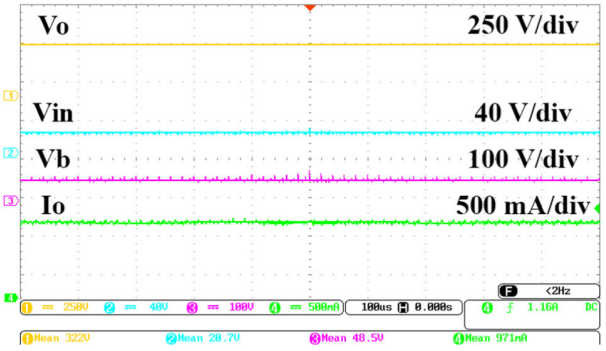

(b)

FIGURE 19. Performance of the converter with high voltage gain when d_1 and d_2 are set on 0.65 (a) the third mode- $P_O = 300W$, $V_{PV} = 19.9V$, and voltage gain = 16.3 (b) the second mode $V_b = 48.5V$, $V_{PV} = 20.7V$, $V_O = 322V$ and $P_O = 312W$.

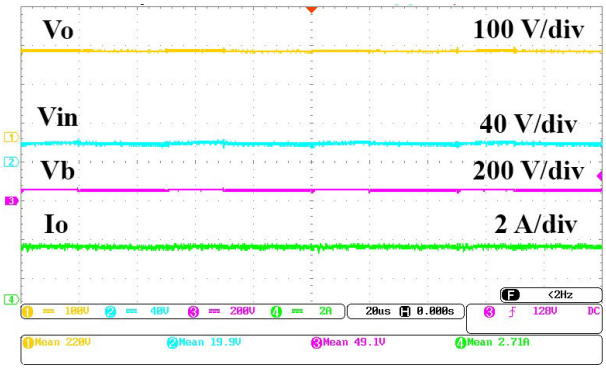

FIGURE 20. Performance of the converter with 600W output power $V_{PV} = 19.9V$, a $V_b = 49.1V$, $V_O = 220$ V.

changing it from 78 dB to 85 dB. Fig. 12 illustrates the Bode diagrams of G_{vd1} and G_{vd3} with and without the controller. The results indicate that in Fig. 12 (a), the phase margin (PM) changes from 110° to 88° with the controller, while the gain margin (GM) improves to 400 dB. Furthermore, in Fig.12(b), it is observed that for G_{vd3}, the phase margin (PM) changes from −60° to 44°, and the gain margin (GM) improves from −28 dB to 51 dB with the controller.

VI. EXPERIMENTAL RESULTS

Fig. 13 depicts the experimental setup consisting prototype of the proposed TPC, the control board and measurement

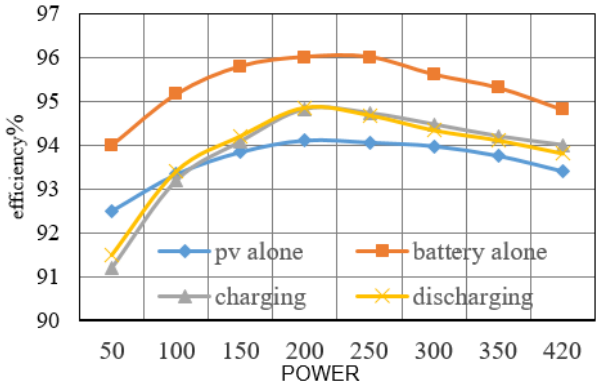

FIGURE 21. Efficiency of the proposed converter per the operation modes for different output power.

equipment. The voltages of the input source, the battery, and the output voltage are set at 20V, 48V, and 255V, respectively. The energy storage comprises lead-acid batteries with series connections. Table 4 provides information on the components that were utilized in the prototype.

Fig.14 displays the results of the experiments performed in the discharging mode (the second mode), including the inductors' current, voltage stress of the switches (S_1 and S_3), and voltage of C_1 and C_3. The results are extracted for input power (P_{PV}) and power of the battery (P_b) equal to 165W and 130W, respectively. According to Fig. 14, the inductor currents have low ripples, and the input current ripple (ripple of L_1) is lower than 40%. All the experiments in steady state condition have good accordance with the kay waveforms in Fig.4 Thus, the main parts of the illustrated results are focused on the dynamic performance of the converter per changing the load, variation of the input source, and switching between the modes. In practice, the PV voltage exhibits a wide range of fluctuations, whereas the battery maintains a relatively constant voltage level. In the experimental results, the voltage characteristics of the PV were taken into account, with variations considered in the range of 20V to 30V. Fig. 15(a) depicts a variation of output power from 230W to 310W, and the controller sets the output voltage, which can be validated by reviewing the results in (Fig. 15(a)). To verify the controller performance, the input voltage is varied from 20V to 30V, and then it returns to its primary state (Fig. 15(b)). Similar to the previous experiment, the results demonstrate the controller's high-speed performance in regulating the battery's current and output voltage.

Fig.16 illustrates the experimental results of the second operation mode with experiment steps like the previous process in Fig. 15. As can be seen, the output voltage is set (the set-point= 255V) with unremarkable changes, the same as the battery's current. Switching between the operations modes by the control algorithm is depicted in Fig. 17, where output power has been changed. In the first step, the input power has a higher value than the load (240W), which causes the battery to charge with extra power.

Then, the load suddenly varied from 240W to 310W, which means equality of the input power and the output

power. Therefore, there is no additional power to charge the battery and the converter operates in no battery contribution mode or the third mode that is managed by the control algorithm. Increasing the load from 310W to 420W causes a supporting lack of power by the battery during the converter operation in the charging mode as shown in the last step of changes (Fig. 17). The changes in the battery current per the steps verify the switching between the modes where the output voltage is controlled appropriately. Furthermore, Figure(Fig. 17) illustrates the application of bidirectional input, allowing the converter to store excess energy and subsequently release it when the PV input is insufficient. By efficiently managing bi-directional energy flow, the overall versatility of the converter can be enhanced. The other important feature of the proposed TPC is its performance in battery-alone mode, causing higher reliability and certainty in supporting output power, especially when the input power is low or equal to zero. Fig.18(a) validates the converter's performance in the battery-alone mode while the output voltage is regulated at 150V. Additionally, Fig. 18(a) demonstrates the controller's high-speed performance when the load fluctuates between 140W and 220W. The results show that the regulation of the output voltage is done perfectly, with an efficiency of more than 93%. As it can be seen in Fig. 18(b), the converter supplies a 230W load with the battery, while the battery current has a low ripple (lower than 30%) and the converter efficiency is 96%. It must be noted that the converter can boost with higher gains in the first, second, and third modes, as depicted in Fig. 14 for two of the modes. Fig. 19(a)shows converter's performance in the third mode for $P_O = 300$W, $V_{PV} = 19.9$V, and voltage gain = 16.3, where d_1 and d_2 are set on 0.65 and the converter's efficiency is 94%. The subsequent in Fig. 19(a)(b) are registered when the voltage of the battery, the input voltage, output voltage, and the output power are 48.5V, 20.7V, 322V, and 312W, respectively. Like the previous mode, the converter transfers the power in this mode with an efficiency equal to 94%. Fig. 20 shows the converter's performance in the second mode(discharging mode) for $P_O = 600$W, $V_{PV} = 19.9$V, and output voltage 220v. The efficiency of the converter is extracted for output power from 100W to 420W (Fig. 21). the battery-alone mode demonstrates the highest efficiency, surpassing all other modes due to lower utilized components. Notably, the charging and discharging modes exhibit superior efficiency compared to the PV alone mode. The converter consistently achieves an efficiency exceeding 93% across various output powers, with an average efficiency of 94% at the nominal output power of 420W. The pinnacle of efficiency is observed in the battery-alone mode, where an output power of 220W corresponds to 96% efficiency. Overall, the converter efficiency levels could be further enhanced by incorporating higher-quality components. Notably, the charging and discharging modes share the same components, resulting in identical efficiencies. Additionally, the PV alone mode has slightly lower efficiency than the other modes, attributed to increased losses due to paths all power in more components. Power losses analysis includes inductor losses(P_L), switching losses(P_{sw}), diode losses(P_D), and capacitors losses(P_{cap}). Each component loss analysis is in the following section.

$$P_{Loss} = P_{sw} + P_{cap} + P_L + P_D \tag{43}$$

The inductor losses $P_L$include core loss (P_{core}), DC conduction loss (P_{LDC}), and AC conduction loss (P_{LAC}), which can be calculated by the equations given in (44) to (48) and current analyses for the inductors. inductor losses due to inductors' magnetic behaviors can be written as (44), which are affected by the inductor's frequency(f), magnetic flux(B), volume(V_e), K is a constant for core material, and x and y are related to the shape of the inductor.

$$P_{core} = Kf^x B^y V_e \tag{44}$$

P_{LDC} for each inductor should be obtained by (45).

$$P_{LDC} = R_{DC} {I_{rms}}^2 = R_{DC}({I_L}^2 + \frac{{\Delta I_L}^2}{3}) \tag{45}$$

Losses of each inductor due to ac resistance can be written as (46)

$$P_{LAC} = R_{AC} {I_{rms}}^2 = R_{AC} \frac{{\Delta I_L}^2}{3} \tag{46}$$

Diode losses(P_D), including conduction loss(P_{dcond}), voltage forward loss (P_{V_D}) and reverse recovery loss ($P_{recovery}$) are summrize as follows.

$$P_{dcond} = R_D {I_{D_{rms}}}^2 \tag{47}$$

$$P_{V_D} = V_D I_{AVG} \tag{48}$$

$$G_{CLin1} = \frac{2.612e09s^7 + 6.538e14s^6 + 3.97e17s^5 + 5.079e22s^4 + 1.43e25s^3 + 1.795e29s^2 + 5.495e29s + 4.195e29}{0.183s^{12} + 108.8s^{11} + 2.845e07s^{10} + 1.606e10s^9 + 1.207e15s^8 + 6.215e17s^7 + 7.894e21s^6 + 2.116e24s^5 + 1.383e28s^4 + 8.467e28s^3 + 3.737e29s^2 + 7.474e29s + 4.95e29} \tag{37}$$

$$G_{CLin2} = \frac{2083s^9 + 2.255e07s^8 + 2.419e11s^7 + 2.543e15s^6 + 6.974e18s^5 + 6.768e22s^4 + 3.645e25s^3 + 2.128e29s^2 + 1.079e30s + 8.054e29}{0.0697s^{12} + 41.71s^{11} + 1.083e07s^{10} + 6.16e09s^9 + 4.598e14s^8 + 2.385e17s^7 + 3.007e21s^6 + 8.179e23s^5 + 5.271e27s^4 + 5.348e28s^3 + 3.883e29s^2 + 1.282e30s + 8.809e29} \tag{38}$$

$$G_{CLvd1} = \frac{-1.577e04s^8 - 8.921e09s^7 - 9.167e13s^6 - 8.288e17s^5 - 7.042e21s^4 - 1.28e25s^3 - 2.64e28s^2 - 3.022e31s - 2.013e31}{7.29e-12s^12 + 8.104e-6s^11 + 2.256s^10 + 2586s^9 + 3.505e08s^8 + 2.403e11s^7 + 1.478e16s^6 + 7.09e18s^5 + 9.007e22s^4 + 1.336e25s^3 + 1.435e29s^2 - 2.999e31s - 2.006e31} \tag{41}$$

$$G_{CLvd3} = \frac{-0.000135^{10} - 69.16s^9 + 3.219e06s^8 - 1.23e10s^7 + 3.49e14s^6 - 3.598e17s^5 + 8.572e21s^4 + 1.351e25s^3 + 3.116e28s^2 + 4.816e31s + 3.209e31}{7.29e-12s^12 + 8.104e-06s^11 + 2.256s^10 + 2517s^9 + 3.537e08s^8 + 2.369e11s^7 + 1.522e16s^6 + 7.559e18s^5 + 1.057e23s^4 + 3.967e25s^3 + 2.011e29s^2 + 4.838e31s + 3.217e31} \tag{42}$$

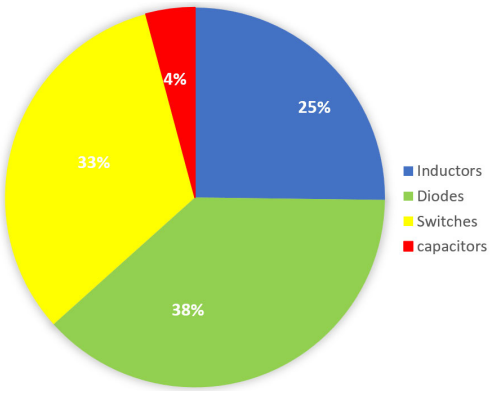

FIGURE 22. Losses distribution in PV-alone mode for 272W output power.

For each diode, losses due to recovery losses $P_{recovery}$ can be written as (49)

$$P_{recovery} = \frac{1}{T}\int_0^T v_d(t)i_d(t)dt \tag{49}$$

The switch's losses P_{sw} include conduction loss (P_{scond}) and switching losses in the converter (P_{sw}). The switching loss is subdivided into turn-on loss (P_{on}) and turn-off loss (P_{off}). P_{sw} can be written as (50)

$$P_{sw} = P_{off} + P_{on} = \frac{V_{DS}I_S F_{SW}(t_{off} + t_{on})}{2} \tag{50}$$

Like diodes, mosfet conduction losses can be formulated as (51):

$$P_{scond} = R_S {I_S}_{rms}{}^2 \tag{51}$$

The losses of the capacitors P_{cap}comprise conduction losses, which can be computed using the RMS current pass-through capacitors and the capacitors' resistance value (Rc). Losses distribution is shown in 22 for pv-alone mode.

$$P_{cap} = R_c(I_{CRMS})^2 \tag{52}$$

Based on the calculations performed in this section, the total circuit losses can be expressed by eq (53). However, due to measurement equipment errors, discrepancies may exist between the calculated values and the measured values.

$$P_{Loss} = P_{sw} + P_{cap} + P_L + P_D = 17.06W \tag{53}$$

The loss distribution is illustrated in Fig. 22. The distribution reveals that diode losses constitute the largest portion of the proposed converter's losses, accounting for 39% of the total losses. Switches contribute to losses following diodes, comprising approximately 33%

VII. CONCLUSION

The proposed TPC boosts voltage with high gain per its operation modes. It is experimented for voltage gain equal to 12.5 in the three modes, while it can be used for higher gains as experimented for V_O/V_{in}=16.3 during the second and third modes. The converter operates with acceptable efficiency for output powers lower than 420W. All the input ports have a common ground with the load. In addition, the input current of the unidirectional port is continuous with a low current ripple. The main advantage of the converter is its battery-alone mode performance, which improves the reliability of the TPC in stand-alone applications. These features were introduced during the converter design process to present a more comprehensive converter in comparison to the previous topologies. According to the applied switching strategy, the converter transitions between the modes simply and appropriately. The results have demonstrated the converter's suitable performance during sudden changes and its stability under various conditions. Based on the advantages of the converter and its superiority over other TPCs, the proposed converter is suitable for renewable energy applications.

REFERENCES

[1] M. Maalandish, S. H. Hosseini, S. Ghasemzadeh, E. Babaei, and T. Jalilzadeh, "A novel multiphase high step-up DC/DC boost converter with lower losses on semiconductors," *IEEE J. Emerg. Sel. Topics Power Electron.*, vol. 7, no. 1, pp. 541–554, Mar. 2019.

[2] S. Asghari-Gorji, A. Mostaan, and H. Javadi, "A new structure of Y-source inverters with continous input current and high voltage gain," in *Proc. 6th Power Electron., Drive Syst. Technol. Conf. (PEDSTC)*, Feb. 2015, pp. 515–520.

[3] V. Abbasi, S. Rostami, S. Hemmati, and S. Ahmadian, "Ultrahigh step-up quadratic boost converter using coupled inductors with low voltage stress on the switches," *IEEE J. Emerg. Sel. Topics Power Electron.*, vol. 10, no. 6, pp. 7733–7743, Dec. 2022.

[4] M. Uno and K. Sugiyama, "Switched capacitor converter based multiport converter integrating bidirectional PWM and series-resonant converters for standalone photovoltaic systems," *IEEE Trans. Power Electron.*, vol. 34, no. 2, pp. 1394–1406, Feb. 2019.

[5] P. Kolahian, H. Tarzamni, A. Nikafrooz, and M. Hamzeh, "Multi-port DC–DC converter for bipolar medium voltage DC micro-grid applications," *IET Power Electron.*, vol. 12, no. 7, pp. 1841–1849, Jun. 2019.

[6] S. Jalilyan, V. Abbasi, S. Ahmadian, A. R. Varmenjeh, and F. Y. Moghadam, "High step-up three-port DC–DC converter with few limitations in performance suitable for stand-alone renewable energy applications," *IEEE Trans. Ind. Electron.*, early access, 2024, doi: 10.1109/TIE.2024.3360616.

[7] Z. Wang, Q. Luo, Y. Wei, D. Mou, X. Lu, and P. Sun, "Topology analysis and review of three-port DC–DC converters," *IEEE Trans. Power Electron.*, vol. 35, no. 11, pp. 11783–11800, Nov. 2020.

[8] K. Varesi, S. H. Hosseini, M. Sabahi, and E. Babaei, "Modular non-isolated multi-input high step-up DC–DC converter with reduced normalised voltage stress and component count," *IET Power Electron.*, vol. 11, no. 6, pp. 1092–1100, May 2018.

[9] K. Varesi, S. H. Hosseini, M. Sabahi, E. Babaei, and N. Vosoughi, "Performance and design analysis of an improved non-isolated multiple input buck DC–DC converter," *IET Power Electron.*, vol. 10, no. 9, pp. 1034–1045, Jul. 2017.

[10] S. Rostami, V. Abbasi, and M. Parastesh, "Design and implementation of a multiport converter using Z-Source converter," *IEEE Trans. Ind. Electron.*, vol. 68, no. 10, pp. 9731–9741, Oct. 2021.

[11] F. Kardan, R. Alizadeh, and M. R. Banaei, "A new three input DC/DC converter for hybrid PV/FC/battery applications," *IEEE J. Emerg. Sel. Topics Power Electron.*, vol. 5, no. 4, pp. 1771–1778, Dec. 2017.

[12] S. Rostami, V. Abbasi, N. Talebi, and T. Kerekes, "Three-port DC–DC converter based on quadratic boost converter for stand-alone PV/battery systems," *IET Power Electron.*, vol. 13, no. 10, pp. 2106–2118, Aug. 2020.

[13] S. Rostami, V. Abbasi, and N. Talebi, "Ultrahigh step-up multiport DC–DC converter with common grounded input ports and continuous input current," *IEEE Trans. Ind. Electron.*, vol. 69, no. 12, pp. 12859–12873, Dec. 2022.

[14] K. Varesi, S. H. Hosseini, M. Sabahi, and E. Babaei, "A high-voltage gain nonisolated noncoupled inductor based multi-input DC–DC topology with reduced number of components for renewable energy systems," *Int. J. Circuit Theory Appl.*, vol. 46, no. 3, pp. 505–518, Mar. 2018.
[15] K. Varesi, S. Hossein Hosseini, M. Sabahi, E. Babaei, S. Saeidabadi, and N. Vosoughi, "Design and analysis of a developed multiport high step-up DC–DC converter with reduced device count and normalized peak inverse voltage on the switches/diodes," *IEEE Trans. Power Electron.*, vol. 34, no. 6, pp. 5464–5475, Jun. 2019.
[16] V. A. K. Prabhala, P. Fajri, V. S. P. Gouribhatla, B. P. Baddipadiga, and M. Ferdowsi, "A DC–DC converter with high voltage gain and two input boost stages," *IEEE Trans. Power Electron.*, vol. 31, no. 6, pp. 4206–4215, Jun. 2016.
[17] R. Cheraghi, E. Adib, and M. S. Golsorkhi, "A nonisolated high step-up three-port soft-switched converter with minimum switches," *IEEE Trans. Ind. Electron.*, vol. 68, no. 10, pp. 9358–9365, Oct. 2021.
[18] H. Wu, K. Sun, S. Ding, and Y. Xing, "Topology derivation of nonisolated three-port DC–DC converters from DIC and DOC," *IEEE Trans. Power Electron.*, vol. 28, no. 7, pp. 3297–3307, Jul. 2013.
[19] R. Faraji, H. Farzanehfard, G. Kampitsis, M. Mattavelli, E. Matioli, and M. Esteki, "Fully soft-switched high step-up nonisolated three-port DC–DC converter using GaN HEMTs," *IEEE Trans. Ind. Electron.*, vol. 67, no. 10, pp. 8371–8380, Oct. 2020.
[20] T. Jalilzadeh, N. Rostami, E. Babaei, and S. H. Hosseini, "Design, analysis and implementation of a new three-port DC–DC converter with bidirectional capability," *IET Power Electron.*, vol. 14, no. 15, pp. 2490–2506, Nov. 2021.
[21] R. Faraji, H. Farzanehfard, M. Esteki, and S. A. Khajehoddin, "A lossless passive snubber circuit for three-port DC–DC converter," *IEEE J. Emerg. Sel. Topics Power Electron.*, vol. 9, no. 2, pp. 1905–1914, Apr. 2021.
[22] B. Honarjoo, S. M. Madani, M. Niroomand, and E. Adib, "Non-isolated high step-up three-port converter with single magnetic element for photovoltaic systems," *IET Power Electron.*, vol. 11, no. 13, pp. 2151–2160, Nov. 2018.
[23] E. Amiri, R. R. Khorasani, E. Adib, and A. Khoshkbar-Sadigh, "Multi-input high step-up DC–DC converter with independent control of voltage and power for hybrid renewable energy systems," *IEEE Trans. Ind. Electron.*, vol. 68, no. 12, pp. 12079–12087, Dec. 2021.
[24] M. Azizi, M. Mohamadian, and R. Beiranvand, "A new family of multi-input converters based on three switches leg," *IEEE Trans. Ind. Electron.*, vol. 63, no. 11, pp. 6812–6822, Nov. 2016.
[25] S. Danyali, S. H. Hosseini, and G. B. Gharehpetian, "New extendable single-stage multi-input DC–DC/AC boost converter," *IEEE Trans. Power Electron.*, vol. 29, no. 2, pp. 775–788, Feb. 2014.
[26] E. Babaei, H. Tarzamni, F. Tahami, H. K. Jahan, and M. B. B. Sharifian, "Multi-input high step-up inverter with soft-switching capability, applicable in photovoltaic systems," *IET Power Electron.*, vol. 13, no. 1, pp. 133–143, Jan. 2020.
[27] R. R. Ahrabi, H. Ardi, M. Elmi, and A. Ajami, "A novel step-up multiinput DC–DC converter for hybrid electric vehicles application," *IEEE Trans. Power Electron.*, vol. 32, no. 5, pp. 3549–3561, May 2017.

SIROOS JALILYAN received the B.S. degree in electrical engineering from Kermanshah University of Technology, in 2016, and the M.S. degree in electrical engineering from Khaje Nasireddin Toosi, Tehran, Iran, in 2020. His current research interest includes the design and implementation of power electronics converter especially multiport dc-dc converter.

VAHID ABBASI received the B.S. degree in electrical engineering from Shahid Chamran University, Ahvaz, Iran, in 2002, and the M.S. and Ph.D. degrees in electrical engineering from Iran University of Science and Technology, Tehran, Iran, in 2004 and 2012, respectively. He is currently an Assistant Professor with the Department of Electrical Engineering, Kermanshah University of Technology, Kermanshah, Iran. His current research interest includes the design and implementation of power electronic converters

ABBAS RAHIMI VARMENJEH received the B.S. degree in electrical engineering-power from Kermanshah University of Technology (KUT), Kermanshah, Iran, in 2016. His current research interest includes the design and implementation of power electronic dc-dc converters with KUT Power Electronics Laboratory.

SINA AHMADIAN received the B.S. degree in electrical engineering from Kermanshah University of Technology, Kermanshah, Iran, in 2020, where he is currently pursuing the M.S. degree in power electronics. His current research interests include design and implementation of power electronic converters, especially multiport inverters.

SAMAN A. GORJI (Senior Member, IEEE) received the B.Sc. and M.Sc. degrees in electrical engineering from the University of Guilan, in 2011 and 2013, respectively, and the Ph.D. degree in electrical engineering from the Swinburne University of Technology, in 2018. He is currently a Senior Lecturer in electrical and renewable energy engineering and a CSIRO International Hydrogen Research Fellow with Deakin University, Australia. Prior to joining Deakin University, he was a Foundation Research Fellow with the Centre for Clean Energy Technologies and Practices, Queensland University of Technology (QUT), and with the Future Energy Exports Cooperative Research Centre (FEnEx CRC). His current research interests include modeling and design of power electronics circuits, efficient power conversion, renewable electrical energy systems, and microgrids for green hydrogen production.